Computation of UH-60A Airloads Using CFD/CSD Coupling On Unstructured Meshes

Robert T. Biedron
Senior Research Scientist

Elizabeth M. Lee-Rausch
Research Engineer

NASA Langley Research Center, Hampton, VA 23681

An unsteady Reynolds-averaged Navier-Stokes solver for unstructured grids is used to compute the rotor airloads on the UH-60A helicopter at high-speed and high thrust conditions. The flow solver is coupled to a rotorcraft comprehensive code in order to account for trim and aeroelastic deflections. Simulations are performed both with and without the fuselage, and the effects of grid resolution, temporal resolution and turbulence model are examined. Computed airloads are compared to flight data.

Nomenclature

$()_{tip}$	value at the blade tip
α	fuselage angle of attack [°]
μ	advance ratio
ψ	azimuthal position, [°]
ρ	density [slugs/ft^3]
σ	solidity
θ_0	collective pitch, [°]
θ_c	negative of lateral cyclic pitch, [°]
θ_s	negative of longitudinal cyclic pitch, [°]
a	speed of sound [ft/s]
c	local blade chord [ft]
C_T	thrust coefficient
F_Z	rotor thrust [lb]
M	Mach number
M^2C_a	$c/4$ sectional axial (chord) force coefficient ($\frac{F_a}{\frac{1}{2}\rho a^2 c}$)
M^2C_m	sectional pitching moment coefficient ($\frac{M_y}{\frac{1}{2}\rho a^2 c^2}$)
M^2C_n	sectional normal force coefficient ($\frac{F_n}{\frac{1}{2}\rho a^2 c}$)
M_X	rotor rolling moment [ft-lb]
M_Y	rotor pitching moment, [ft-lb]
R	rotor radius, [ft]
r	radial position, [ft]
BDF	Backward Differentiation Formulae
BL	baseline mesh
CAMRAD II	Comprehensive Analytical Model of Rotorcraft Aerodynamics and Dynamics II
CFD	Computational Fluid Dynamics
CO	coarse mesh
CSD	Computational Structural Dynamics
HRLES	Hybrid Reynolds-Averaged Navier-Stokes/Large-Eddy Simulation turbulence model
RB	refined-blade mesh
SA	Spalart-Allmaras turbulence model
SST	Shear Stress Transport turbulence model

Presented at the American Helicopter Society 67th Annual Forum, Virginia Beach, VA, May 3-5, 2011.

Introduction

The prediction of rotorcraft airloads presents a significant challenge for Computational Fluid Dynamics (CFD). The combination of complex flow physics, nonlinear structural dynamics, and the geometrical complexity of rotorcraft all must be accounted for. Significant progress has been made in the last decade toward meeting this challenge. Potsdam et al. (Ref. 1) combined the structured-grid CFD code OVERFLOW (Ref. 2) with the rotorcraft Computational Structural Dynamics (CSD) code CAMRAD II (Ref. 3) in a loosely-coupled fashion and applied the coupled system to the UH-60A Blackhawk helicopter. A code such as CAMRAD II is also referred to as a 'comprehensive' code, because in addition to structural dynamics models, aerodynamic, propulsion, and trim models are provided. In a coupled CFD/CSD system, the CFD solver replaces the aerodynamic analysis of the comprehensive code, while the CSD code continues to provide the structural dynamics and trim. The generally good comparison with flight-test data obtained in Ref. 1 renewed interest in the loose-coupling approach originally proposed by Tung et. al (Ref. 4). Indeed, the loose-coupling method has now been applied by many other researchers, not only to the UH-60A, but to other configurations as well.

Most of the CFD/CSD work to date has been performed using structured-grid CFD solvers. Structured-grid solvers are generally very efficient in terms of computational resources, but for complex geometries, the human effort required to generate the requisite grid systems can be significant. Unstructured-grid CFD solvers require greater computational resources, but the human effort to generate grids about complex geometries is typically far less. As a result, the total time to solution can be less for unstructured-grid solvers. In Reference 5, the unstructured-grid CFD solver FUN3D (Ref. 6) was loosely coupled to the CAMRAD II code and applied to the HART-II configuration for three test conditions. Abras (Ref. 7) coupled the FUN3D solver to the DYMORE CSD code and applied the resulting system to UH-60A high-speed and low-speed flight conditions. Sankaran et al. (Ref. 8) used a novel unstructured/cartesian hybrid solver coupled with the RCAS comprehensive code to compute rotor airloads for several UH-60A flight conditions.

In this paper, we apply the FUN3D/CAMRAD II analysis system to the UH-60A for two flight conditions, one high-speed and the other high-thrust. The UH-60A database (Refs. 9, 10) has an extensive range of aerodynamic and structural-loads data at numerous flight conditions across the flight envelope and thus provides a very useful data set for validation of computational results. The focus here is on the validation of computed rotor airloads, and the assessment of the sensitivity of the airloads to several CFD-related inputs: grid size, turbulence model, and time step. The sensitivities of the off-body aerodynamics (e.g. vortex propagation) to these variations is not considered. Although the emphasis is on aerodynamics, because the aerodynamics and structures do interact with one another some comparisons of structural loads from flight and computation are also presented. However, no attempt is made to assess the sensitivity of the results to any structural-modeling input.

CFD/CSD Methodology

The unstructured-grid flow solver used for this study is FUN3D. The code solves the Navier-Stokes equations, including the full viscous terms (i.e. the thin-layer assumption is not made), with several turbulence modeling options. FUN3D is a node-centered code, so that the number of unknowns is directly related to the number of nodes in the grid. The code supports 'mixed-element' meshes in which the nodes may be connected into prismatic, hexahedral, or pyramidal elements instead of, or in addition to, tetrahedra. The solver has a variety of mesh-motion options, including rigid, deforming, and overset meshes, and a robust implicit time-advancement scheme (Ref. 11). For overset meshes, the DiRTlib (Ref. 12) and SUGGAR++ (Ref. 13) codes are used to facilitate communication between disparate zones in the mesh. These features make the solver attractive for rotorcraft applications, where the flow is fundamentally unsteady and the flexible rotor blades undergo large motions relative to the fuselage. O'Brien (Ref. 14) first applied the FUN3D solver to rotorcraft simulations, with the restriction of rigid blades with prescribed motion. Subsequent modifications resulted in a more general rotorcraft capability, with the ability to account for aeroelastic effects and trim via coupling with the CAMRAD II rotorcraft comprehensive code (Ref. 5). The coupling is implemented via the loose coupling strategy outlined in Ref. 1, and thus is appropriate to steady, level flight.

The rotorcraft CSD code used for this study is CAMRAD II. The aerodynamics modules within CAMRAD II are based on lifting-line models utilizing airfoil tables, coupled with wake models. Although such aerodynamic models can provide reasonable results for many flight conditions, in some cases the predictions of the airloads can be inaccurate because of limitations of the relatively low-order aerodynamic modeling. The goal of the loose coupling approach is to replace the low-order lifting-line aerodynamics of the CSD code with the higher-fidelity Navier-Stokes aerodynamics of the CFD code. Within CAMRAD II, each blade is modeled as a set of nonlinear beam elements. In addition to the structural dynamics modeling, CAMRAD II offers a sophisticated trim capability. For the UH-60A simulations in this paper, a three-degree-of-freedom trim is utilized, with the (solidity-weighted) thrust coefficient, pitching moment and rolling moment specified as trim targets within CAMRAD II.

In the loose coupling approach, airloads data from the CFD solver and blade motion data from the CSD solver are exchanged at relatively infrequent periodic intervals, for ex-

ample once per revolution or more generally once per integer multiple of the blade passage. In a typical coupled simulation, the initial execution of FUN3D is carried out for two complete rotor revolutions, using blade deformations from a trimmed CAMRAD II solution with unmodified lifting-line aerodynamics. In subsequent coupling cycles, FUN3D is run for two blade passages between coupling cycles (i.e. one-half revolution for a four-bladed rotor such as the UH-60A). Although coupling could be performed as frequently as each blade passage, running the solver for the extra blade passage helps damp out transients between coupling cycles. This coupling strategy has not been examined for optimality; however, it has proven to be a robust strategy (stable and convergent). The coupled system is tied together by separate interface codes that perform data translation between FUN3D and CAMRAD II. A shell script is used to orchestrate the execution of the various codes, and to provide restart, post-processing, and archiving functions.

CFD Grids

The baseline composite-grid systems for the isolated UH-60 rotor were developed by over-setting component grids for each individual blade with an empty (background) square domain. The component unstructured grids for the overset computations were generated with the VGRID v4.0 advancing-layer and advancing-front grid generation software package (Ref. 15). The grids generated with VGRID were fully tetrahedral. However, VGRID uses an advancing-layer technique to generate the boundary-layer portion of the grid so that prisms can be reconstructed in the boundary layer for use with a mixed-element discretization. In the boundary layer, three tetrahedral cells are combined into one prism. The mixed-element grids have essentially the same number of nodes and nodal spacing as the fully-tetrahedral grids although the number of cells and the shape of the control volumes differ in the boundary layers.

The blade surface geometry used for grid generation is based on an updated definition provided by the Sikorsky Aircraft Corporation via the UH-60 Airloads Workshop in May 2009. The updated geometry includes more spanwise resolution at the tip cap and a correction to the spanwise location of the trim tab. The near-body blade grid extends away from the blade to a cylindrical outer boundary of radius $1.5c_{tip}$. In the wall normal direction, the grid spacing is set such that an average normalized coordinate y^+ is less than one for the first grid cell at the wall for the majority of the blade. The maximum spacing at the blade grid outer boundary is approximately $0.10c_{tip}$. The characteristic spacings of the baseline rotor grid are summarized in Table 1. Note that these are the spacing values associated with the VGrid "sources" which are used to control the unstructured grid spacing field, rather than the actual spacings between node points, though they are loosely correlated. The maximum spanwise stretching is 30:1 near both the blade leading edge (LE) and trailing edge (TE). The surface grid has approximately 5 points across the blunt trailing edge. Each component blade grid has approximately 2.65 million nodes. Figures 1(a)–(c) show a comparison of the surface mesh near the tip of the rotor blade for the coarse, baseline and refined blade grids. Figures 1(d)–(f) show the corresponding slices taken through the blade volume grids at the $r/R = 0.865$ radial station which is at the outboard edge of the trim tab.

	Direction	Characteristic Spacing
Blade Surface	chordwise	$0.0029c$ LE
		$0.0014c$ TE
	spanwise	$0.0009R$ Root
	at mid-chord	$0.0056R$ Mid-Span
		$0.0009R$ Tip
	normal	$2.62 \times 10^{-6} c_{tip}$
		(geometric stretching 1.20)
Blade Outer Boundary	isotropic	$0.10c_{tip}$

Table 1. Characteristic spacings of baseline blade grid.

The off-body grid (background grid) for the isolated rotor is defined in a square box whose sides extend $5R$ out from the rotor hub. The finest spacing in the off-body grid is approximately $0.10c_{tip}$. This minimum spacing is maintained, within the constraints of the unstructured meshing software, in a cylindrical volume which extends $1.1R$ in the blade plane and $0.20R$ above and $0.20R$ below the blade plane. This cylindrical volume of refinement was achieved by utilizing VGrid volume sources (Ref. 16). The background component grid has approximately 7.0 million nodes. The baseline composite grid has a total of approximately 17.6 million nodes. A slice through the baseline isolated UH-60 composite grid in Fig. 3 shows the spacing characteristics of the blade and off-body grids through the computational domain. The grids are shown in a vertical plane passing through the rotor hub location. Note that the fringe and hole points are not plotted.

Although a mathematically consistent grid refinement study in the sense of Ref. 17 was not performed, alternative composite-grid systems were developed to look at the effects of grid refinement: a globally coarsened grid and a refined blade grid. A comparison of global characteristics for these composite grids is provided in Table 2. The coarse composite grid was developed from the baseline grid by increasing the minimum off-body mesh spacing to $0.20c_{tip}$ and increasing the baseline grid surface spacings by a factor of 1.3. This coarse composite grid has approximately 6.9 million nodes. A refined blade grid was developed by globally refining the blade surface-grid spacings by a factor 0.73. The maximum spacing at the blade grid outer boundary was set to $0.10c_{tip}$ so that this grid could be overset with the baseline off-body grid.

		Baseline	Coarse	Refined Blade
Blade Grid	Nodes (millions)	2.7	1.3	7.6
	Viscous Surface Nodes (thousands)	62	33	126
	Surface Spacing Factor	1	1.3	0.73
	Wall Normal Spacing Factor	1	1.3	1.00
	Characteristic Outer Boundary Spacing	$0.10c_{tip}$	$0.20c_{tip}$	$0.10c_{tip}$
Background Grid	Nodes (millions)	7.0	1.8	7.0
	Finest Spacing	$0.10c_{tip}$	$0.20c_{tip}$	$0.10c_{tip}$
	Outer Boundary Extent	5R	5R	5R
Composite Grid	Total Nodes (millions)	17.6	6.9	37.4

Table 2. Comparison of composite grid systems.

An off-body grid containing the UH-60 fuselage body was developed to study the influence of the body aerodynamics on the rotor airloads. The fuselage surface geometry was provided by Sikorsky Aircraft Corporation. The rotor hub, shaft, and blade linkages are not modeled, nor is the tail rotor modeled. Figure 2 shows the surface mesh for the fuselage and the baseline rotor grid. The surface mesh for the fuselage body has 59,000 nodes. In the wall normal direction, the grid spacing ($3.80 \times 10^{-7} c_{tip}$) is set such that an average normalized coordinate y^+ is less than one for the first grid cell at the wall for the majority of the body. The outer boundary of the fuselage grid is a square box whose sides extend $5R$ out from the rotor hub. This grid also contains a cylindrical volume of refinement in the vicinity of the rotor plane of motion similar to the one defined for the isolated rotor. The maximum spacing within this cylinder is not allowed to exceed $0.10c_{tip}$. The fuselage component grid has approximately 8.4 million nodes. When the fuselage grid is combined with the baseline rotor blades, the resulting composite grid has a total of approximately 19.2 million nodes. A slice through the baseline rotor/fuselage composite grid in Fig. 3 shows the spacing characteristics of the blade and off-body grids through the computational domain. The grids are shown in a vertical plane passing through the fuselage centerline (the fringe and hole points are not plotted). Note that when the fuselage is included, the rotor is inclined at the shaft angle, while for the isolated rotor, the rotor is not inclined, and the shaft angle is accounted for in the specified angle of attack.

For all composite grid systems, SUGGAR++ is used in a pre-processing step to create the composite grid and the domain connectivity file (DCI) for the nominal rotor position. For dynamic overset cases, the DCI file is created at each time step (azimuthal location) by calling a set of SUGGAR++ library routines directly from FUN3D. SUGGAR++ offers a selection of hole-cutting algorithms. For this work, the direct-cut method was used to define the blanked points in the composite grid, and an overlap minimization process was used to identify fringe points. A donor quality value of 0.9 was specified, and no orphans were generated in the overlap process for the baseline and refined-blade grids. The overlap process for the coarse grid generated a small number of orphans (on the order of a few dozen) during part of the rotor revolution.

Computational Results

Most results presented here are obtained using a standard set of input parameters for CFD modeling. This standard or "best practices" set has emerged over the course of numerous rotorcraft simulations using the FUN3D solver. The standard computation utilizes a mixed-element mesh with prisms in the boundary layers near solid surfaces, and tetrahedra elsewhere. Inviscid fluxes are evaluated with a second-order (in space) implementation of Roe's scheme (Ref. 18). The standard turbulence model is the Spalart-Allmaras turbulence model (Ref. 19). The turbulence model is applied to both the near-body and off-body regions. For the present results, no rotational corrections to the turbulence model are utilized. Time advancement is carried out with a modified second-order backward-difference dual-time scheme which results in reduced leading-order truncation error compared to the classical second-order backward-difference scheme (Refs. 20, 21). The standard time step corresponds to a 1° change in blade azimuth per step. Time advancement is performed under the guidance of a 'temporal error controller' (Refs. 11, 20) in which dual-time subiterations are carried out within each time step until either the L_2 norm of the nonlinear residual is reduced to a specified fraction of the estimated temporal error, or, a specified maximum number of subiterations have been performed. For the results presented here, the error fraction ranges from 0.005 to 0.01, and the maximum number of subiterations allowed ranges from 40 to 60.

To assess the sensitivity of the computed results to several important CFD "parameters", variations from the standard set described above are examined. The effect of cell topology is considered by using both tetrahedral and mixed-element grids. The effect of mesh refinement is considered by performing isolated-rotor simulations using the coars-

ened, baseline, and refined-blade grids described above, with resolutions ranging from 6.9 to 37.4 million nodes. The influence of the fuselage on the rotor airloads is examined by replacing the empty-box background grid of the baseline isolated-rotor mesh with one containing the fuselage, leaving the rotor grids unchanged. Sensitivity to time step is examined using a step which corresponds to a 0.5° change in blade azimuth per step. Two additional turbulence models are considered: the Shear Stress Transport (SST) model of Menter (Ref. 22) and a hybrid model that combines the SST model near walls with a Large Eddy Simulation (LES) model of the subgrid-scale turbulent kinetic energy (Ref. 23).

The two flight conditions considered in this paper are denoted as counters 8534 and 9020, and represent high-speed and high-thrust conditions, respectively. Table 3 summarizes the flight conditions and trim targets used for the simulations. Within CAMRAD II, the thrust target is specified via the solidity-weighted thrust coefficient while the pitch and rolling moment targets are specified directly. The rotor is tilted relative to the fuselage by -3° (forward tilt, see Fig. 3). This tilt is accounted for in the angle of attack used in the simulation when running isolated rotor analyses.

Figure 4 illustrates the radial stations at which flight-test data were collected on one of the rotor blades. Here, airloads are presented at a subset of these measurement stations, with comparison of flight data and computed results for normal force, pitching moment, and chord force vs. blade azimuth at selected stations. The zero position for blade azimuth is defined as that for which the blade is nominally aligned with the fuselage axis, pointing aft. Computational results for forces and moments include both pressure and skin-friction contributions, whereas flight data only include pressure contributions. The plots at each selected station are presented in a triptych format, which makes it easy to see the simultaneous effects of an 'event', such as dynamic stall, on all three quantities. Sectional airloads at each radial station are presented in nondimensional form, with freestream speed of sound used as the reference velocity - e.g. M^2C_n. Note that means are removed from the sectional airloads plots. It is known that there are discrepancies in some of the flight data due to faulty pressure taps. Plotting data with the means removed masks some of these discrepancies and facilitates assessment of the computational trends relative to flight. However, mean airloads (averaged around the rotor disk) are also compared as a function of radius in order to assess the agreement of the absolute levels. The sectional airloads plots are used to illustrate the sensitivity of the computed results to changes in CFD parameters. To keep the number of figures to a manageable level, most plots are structured to show the sensitivity of the airloads (means removed) to the particular parameter under consideration at two of the nine radial stations, along with the sensitivity of the mean airloads as a function of radius. The two stations chosen are either the two showing the most sensitivity, or one showing the most sensitivity and one showing a typical level of sensitivity.

Counter 8534: High-Speed Condition

Flight counter 8534 has become a canonical case for CFD/CSD validation, so that condition is considered first. This flight condition represents the highest level-flight speed in the UH-60A Airloads Database, as well as the flight condition with the highest vibration levels. The salient features for this flight condition are given in Table 3.

To examine the effects of mesh size, computations on three different mixed-element meshes, containing between 6.9 million to 37.4 million nodes, are shown in Figure 5 for an isolated rotor. The top section of Figure 5 shows the variation of airloads with azimuth angle for station $r/R = 0.965$, while the mid section shows the variation at $r/R = 0.990$ and the bottom section illustrates the mean (azimuthally averaged) variation with radius. The level of differences observed at station $r/R = 0.965$ are typical of differences seen at other stations. By far the largest differences are observed near the tip at $r/R = 0.99$. Mesh refinement has virtually no effect on the mean airloads. Similarly, time-step refinement, shown in Figure 6, shows no effect on the rotor airloads as the step is reduced from the standard value of 1.0° to 0.5°. In a recent paper by Sitaraman et al. (Ref. 24), using feature-based off-body adaption, a similar lack of sensitivity of rotor airloads to mesh refinement was observed for the high-speed (C8534) flight condition.

It should be noted that trim targets for rotor thrust and pitch/roll moments used in the CFD/CSD coupling process are indirectly generated from flight data using estimates of the vehicle gross weight, tail plane loads, and fuselage loads. They are not obtained by integration of the measured sectional loads. Thus differences in the mean sectional airloads and moments between computation and flight do not indicate that the specified trim targets are not met.

Figure 7 shows the comparison of data and computed results for an isolated rotor obtained using both a fully-tetrahedral mesh and a mixed-element mesh. Both meshes have identical point distributions, approximately 17.6 million nodes. With means removed, the variation of the computed airloads with blade azimuthal angle generally agree well with the flight data. Other stations show similar levels of agreement between flight data and computation. Very little difference is observed in the computed results on the two meshes for this flight condition. The largest differences are seen near the rotor tip, where the mixed-element mesh result matches the data slightly better than the tetrahedral mesh. In fact at $r/R = 0.990$ the results on the 17.6 million node tetrahedral mesh are nearly identical to the results on the coarsest mixed-element mesh shown in Figure 5. For all other stations not shown, the differences between the

Counter	$\alpha(deg)$	μ	M_{tip}	C_T/σ	M_Y (ft-lb)	M_X (ft-lb)
8534	−4.31	0.364	0.642	0.081	−4169	−6042
9020	2.49	0.245	0.669	0.118	−2176	−616

Table 3. Flight conditions and trim targets; sign conventions: α + nose up, M_Y + nose up, M_X + right side down.

tetrahedral mesh results and the mixed-element mesh results are very small indeed, comparable to the differences observed at $r/R = 0.865$. Considering the mean airloads (averaged around the rotor disk) as a function of radius, the normal force is reasonably well predicted, the pitching moment less so, and the chord force is poorly predicted past $r/R = 0.40$. The flight data for both pitching moment and chord force exhibit a significant amount of variation from station to station past $r/R = 0.40$. The computational results exhibit much less station-to-station variation than the flight data, although the trends past $r/R = 0.80$ appear similar. The use of the mixed-element grid results in slightly better agreement in the mean chord force along the blade. The mean normal force and mean pitching moment are virtually indistinguishable between the two computations.

The effect of the fuselage is shown in Figure 8 at the two innermost radial stations. Although not shown, the effect of the fuselage on the airloads for $r/R > 0.5$ is much less significant than at stations inboard. For the innermost stations, inclusion of the fuselage results in a general improvement in the correlation between computation and flight data over the forward part of the rotor disk, particularly for the chord force and pitching moment. No substantial change in the correlation with flight data over the aft portion of the rotor disk is obtained by including the fuselage; this area may be more strongly influenced by the hub (not included in the present computations). The mean airloads show virtually no sensitivity to the presence of the fuselage for the outboard sections of the blade, and only minimal differences for the inboard stations.

Next, for an isolated rotor, using the baseline, mixed-element grid, variations of turbulence model (SA, SST and HRLES) are considered. Results are shown for stations $r/R = 0.965$ and $r/R = 0.99$ in Figure 9. Most surprisingly, none of the turbulence models, for this flight condition, produced any noticeable change in the computed results. Although the mesh is fairly fine and relatively isotropic in the region of the rotor disk, it is an open question whether the grid is fine enough, and the time step small enough, to best exploit the the HRLES model.

Table 4 summarizes the sensitivity of the blade control angles required for trim of the rotor to the various CFD parameters discussed above. As expected from the lack of sensitivity of the airloads for this flight condition, the control angles show very little change with parameter variation, a few tenths of a degree at most. In addition, Table 4 summarizes the sensitivity of the computed thrust and torque coefficients to CFD parameter variation. Taking the baseline, mixed-element mesh for the isolated rotor as the reference result, over the range of parameters considered, thrust varies by no more than 0.3 percent, and torque varies by no more than 3.5 percent.

Next the structural loads computed within the coupled CFD/CSD process are compared with those obtained from flight. The UH-60A database contains measured data for torsional moments, normal (flap) moments, and edgewise (chordwise) moments at several stations not coincident with the airloads stations. Figure 10 shows the comparison of computed and measured torsion moment at four radial stations, while Figures 11 and 12 show normal and edgewise bending moments, respectively. The results are shown for the baseline, mixed-element mesh for an isolated rotor, the corresponding tetrahedral mesh, and the mixed-element mesh with the fuselage, all with 1° time step and the SA turbulence model. Of the CFD parameter variations considered, these three cases span the range of variation in the structural loads. As with the airloads, means have been removed. In Figure 10, the torsional moment at $r/R = 0.0466$ has been obtained indirectly from the pitch-link load and the pitch-link load offset of $0.0224R$; the same procedure was done for both flight and computation. In general, the 1/rev variation of torsional and normal-bending moments are reasonably well predicted by the computation. Higher harmonics are not well captured, especially for the flap-bending moment at $r/R = 0.113$. Overall the edgewise bending moments are rather poorly predicted, even for the lowest harmonic. As suggested by the airloads predictions, the structural loads show the most sensitivity to the inclusion of the fuselage, although the influence of the fuselage on the results is small.

Counter 9020: High-Thrust Condition

Flight counter 9020 represents a high-thrust condition at a moderate advance ratio; the conditions for this counter are summarized in Table 3. The high-thrust level leads to dynamic stall for several radial stations on the retreating side.

Mesh refinement was also carried out for counter 9020. For this counter, unlike counter 8534, acceptable iterative convergence during each time step was typically not obtained using a step of 1° on the refined blade grid. For that mesh, with a step of 1°, convergence at nearly all time steps would "hang", and fail to reach the specified temporal error tolerance (0.01 times the residual norm); because

Mesh	Time Step	Turb. Model	θ_0	θ_{1c}	θ_{1s}	C_T	C_Q
CO-mix-iso	1.0°	SA	13.51	2.47	−8.99	0.00688	0.000703
BL-mix-iso	1.0°	SA	13.40	2.42	−8.94	0.00688	0.000682
RB-mix-iso	1.0°	SA	13.37	2.42	−8.95	0.00688	0.000675
BL-tet-iso	1.0°	SA	13.44	2.49	−8.97	0.00688	0.000706
BL-mix-iso	0.5°	SA	13.42	2.42	−8.97	0.00688	0.000683
BL-mix-iso	1.0°	SST	13.42	2.43	−8.95	0.00688	0.000681
BL-mix-iso	1.0°	HRLES	13.41	2.43	−8.96	0.00688	0.000685
BL-mix-fuse	1.0°	SA	13.51	2.71	−9.30	0.00690	0.000673

Table 4. Sensitivity of control settings (measured at pitch hinge), thrust, and torque with respect to CFD parameter variation, Counter 8534. CO: 6.9 million nodes (coarse), BL: 17.6 million nodes (baseline), RB: 37.4 million nodes (refined blade).

the convergence stalled, further subiterations did not lead to additional reduction in the residual. Reducing the time step to 0.5° rectified these convergence issues. As a result, mesh refinement was performed using a time step of 0.5°, to maintain an "apple-to-apples" comparison.

Figure 13 shows the effect of mesh refinement at $r/R = 0.865$ and $r/R = 0.920$ for an isolated rotor, along with the corresponding flight data. Two dynamic stall events are observed at these stations. Near $\Psi = 270°$, the lift drops precipitously, accompanied by a large negative pitching moment and reduction in chord force. After the first event, the lift builds again, until a second stall occurs near $\Psi = 330°$. In general, the phase of these stall events is in good agreement with the flight data, although the magnitudes (particularly pitching moment) differ from those observed in flight. Overall the effect of mesh refinement for counter 9020 is small, although some local effects are significant. Figure 13 shows that while the first stall at $r/R = 0.865$ is unchanged when using the refined blade grid, the magnitude of the pitching moment drop is adversely impacted relative to the data for the second stall. At $r/R = 0.920$, the already delayed (relative to flight) second stall is delayed further, although the magnitude of the change in pitching moment when stall does occur is relatively unchanged. These two stations reflect the largest changes for this condition with mesh refinement; mean values are virtually unchanged. The results from Sitaraman et al. (Ref. 24) using feature-based off-body adaption also indicate a similar sensitivity of rotor airloads to mesh refinement for a related high-thrust (C9017) flight condition.

Figure 14 shows that for the baseline mesh, temporal refinement from 1° per time step to 0.5° per time step produced very little change in the computed results. The primary effect of the smaller time step was to reduce some of the high-frequency oscillations observed after the dynamic stall events in the computed results, particularly for the pitching moment. This is most evident at station $r/R = 0.920$ in Figure 14. There is no significant effect on the mean airloads.

Figure 15 shows computed results, for the isolated rotor, at stations $r/R = 0.865$, and $r/R = 0.920$ for the baseline mesh size using both mixed elements and pure tetrahedra. In this high-thrust case, more differences appear between the fully-tetrahedral mesh and the mixed-element mesh than were observed in the high-speed case. Focusing on the pitching moment at $r/R = 0.865$, both grid topologies capture the two stall events reasonably well. The tetrahedral mesh leads to the first stall event occurring slightly early, while with the mixed-element mesh the onset of stall matches the flight data. Both meshes show a larger drop in pitching moment than the data, with the mixed-element mesh having a slightly larger reduction in pitching moment during the stall. For the second dynamic stall, the trend with mesh topology is reversed - the tetrahedral mesh exhibits a larger reduction in pitching moment. Considering station $r/R = 0.920$, the mixed-element mesh leads to a first stall that is in very good agreement with the data; the tetrahedral mesh again results in an early stall, with a significantly larger drop in pitching moment. As for station $r/R = 0.865$, the tetrahedral mesh results in the second stall occurring virtually at the same azimuthal location as flight, with reasonably good agreement with flight for the magnitude of the drop. On the other hand, the mixed-element mesh results in the second stall occurring approximately 12° too late, with a noticeably smaller reduction in moment.

Turning to the variation of the mean airloads with radius, the two meshes lead to nearly identical results for normal force, with slightly larger differences in pitching moment and chord force. The peak normal force, which occurs near $r/R = 0.865$ in the data, is underpredicted in the computations. It would appear that there are some anomalies in the flight data near $r/R = 0.400$, since the normal force at that station is significantly different than neighboring radial locations, and the chord force there is off the scale of the plot. Interestingly, the flight data for pitching moment at $r/R = 0.400$ does not appear to be out of line with nearby radial locations.

Next, the effects of including the fuselage are considered. Compared with the high-thrust case, including the fuselage has a generally smaller effect on the results, but

including the fuselage does not consistently improve the comparison with data. For example, Figure 16 shows the effect of the fuselage on the airloads at $r/R = 0.400$ and $r/R = 0.675$. At $r/R = 0.400$, inclusion of the fuselage improves the correlation with the flight data for the normal force and chord force. While inclusion of the fuselage changes the pitching moment, the addition cannot be said to affect the overall level of agreement with flight. At $r/R = 0.675$, including the fuselage results in a markedly reduced drop in pitching moment near $\psi = 240^\circ$, while the overall comparison with normal force and chord is neither better nor worse. The computed mean airloads for this flight condition are virtually unchanged when the fuselage is included.

Because mesh refinement for flight counter 9020 showed some sensitivity to mesh size, turbulence model variations were conducted on the refined blade grid. Furthermore, because the refined blade grid exhibited poor convergence with the larger time step, a time step corresponding to 0.5° azimuth change per step was used for the turbulence model variations. Figure 17 shows the comparison of the SA, SST, and HRLES models at stations $r/R = 0.865$ and $r/R = 0.920$. These radial stations show the most variation between models over all the nine flight-data stations. At $r/R = 0.865$, all three models pick up the proper phase for the first stall. The SST model does a very good job at predicting the magnitude of the pitching moment through the first stall, while both SA and HRLES predict a larger negative pitching moment than indicated by the flight data. At $r/R = 0.865$ all three models predict the second stall to some degree, although once again it is the SST model that does the best job with the level of pitching moment change. At $r/R = 0.920$, only the SST model shows the slightest hint of the second stall event. The mean airloads are virtually unaffected by the various turbulence models.

The sensitivity to CFD parameters of the trim control angles and the rotor thrust and torque are listed in Table 5. Compared to the high-speed case, more variation in the results for the torque coefficient are observed when the parameters are varied. Taking the baseline, mixed-element mesh for the isolated rotor as the reference result, over the range of parameters considered, thrust varies by no more than 0.3 percent, whereas torque varies by as much as 13.5 percent.

Finally, Figure 18 shows the comparison of computed and measured torsion moment at four radial stations, while Figures 19 and 20 show the normal and edgewise bending moments, respectively. The results are shown for the baseline, mixed-element mesh for the isolated rotor, the corresponding tetrahedral mesh, and the tetrahedral mesh with the fuselage, all with 1° time step and the SA turbulence model. As for the high-speed case, overall variation is reasonably well predicted for the torsion and normal bending moments, with higher-harmonics being less well predicted, especially for normal bending at $r/R = 0.113$. Edgewise bending shows little agreement with data, although for this flight condition, clipping is evident in the flight data. As expected from the airloads results, little sensitivity to CFD parameter variation is evident in the structural loads.

Summary

A fully unstructured RANS solver has been used to compute rotor airloads for the UH-60A helicopter, for the purpose of validating the solver against the flight database. Two flight conditions, corresponding to high-speed and high-thrust conditions were examined. Parametric variations of the computed results to mesh size, time step, and turbulence model were considered in the CFD model; the structural model was held fixed in all cases. Remarkably, the high-speed case exhibited virtually *no* sensitivity to any of the variations in computational inputs, except for the inclusion of the fuselage. Although the unsteady (i.e. mean removed) variation of the computational results showed reasonably good agreement with flight data, there were differences between computation and flight that were not impacted by variation of the computational input. Furthermore, the agreement between computation and flight for the mean loads was not nearly as good as for the unsteady loads. Likewise, the agreement between computation and flight for the mean loads was not significantly influenced by computational variation. There are a number of results from CFD/CSD computations for Counter 8534 in the literature, for example fully structured-grid results of Reference 1 and the hybrid unstructured/Cartesian results of Reference 24. The fully unstructured results presented in this paper are virtually identical to results in the cited references. While the high-speed case showed no sensitivity to CFD-model variations, the high-thrust case did show some sensitivity, the largest being with respect to the second of two dynamic stall events on the retreating side.

The relatively small changes in computational results with changes in important CFD modeling parameters (mesh size, turbulence model, and time step) may suggest that the observed differences with flight data are not wholly due to errors in CFD modeling, and that perhaps the structural modeling needs to be examined. Of course there are still areas lacking in CFD modeling. While a reasonably detailed model of the fuselage was included in the computations, the rotor hub and associated linkages, were not modeled, nor was the tail rotor. These missing components may well influence the flow over the rear of the rotor disk. However, they are unlikely to account for discrepancies between computation and flight elsewhere on the rotor disk.

Acknowledgment

The authors would like to thank Mr. William T. Jones of the Computational AeroSciences Branch at NASA Langley for applying his geometry modeling expertise to the

Mesh	Time Step	Turb. Model	θ_0	θ_{1c}	θ_{1s}	C_T	C_Q
CO-mix-iso	0.5°	SA	11.15	3.01	−7.81	0.00996	0.000540
BL-mix-iso	0.5°	SA	10.74	2.73	−7.43	0.00996	0.000547
BL-tet-iso	1.0°	SA	11.12	2.92	−7.89	0.00993	0.000621
RB-mix-iso	0.5°	SA	10.78	2.71	−7.51	0.00997	0.000551
RB-mix-iso	0.5°	SST	10.91	2.84	−7.64	0.00997	0.000577
RB-mix-iso	0.5°	HRLES	10.65	2.72	−7.27	0.00997	0.000539
BL-tet-fuse	1.0°	SA	10.91	3.07	−7.98	0.00996	0.000601

Table 5. Sensitivity of control settings (measured at pitch hinge), thrust, and torque with respect to CFD parameter variation, Counter 9020. CO: 6.9 million nodes, BL: 17.6 million nodes, RB: 37.4 million nodes

fuselage and rotor blade definitions graciously provided by Mr. T. Alan Egolf of the Sikorsky Aircraft Corporation. In addition, we thank Dr. Hyeonsoo Yeo of the U.S. Army Aeroflightdynamics Directorate for providing the CAMRAD II input files.

References

[1]Potsdam, M., Yeo, H., and Johnson, W., "Rotor Airloads Prediction Using Aerodynamic/Structural Coupling," American Helicopter Society 60^{th} Annual Forum Proceedings, 2004.

[2]Nichol, R., Trammel, R., and Buning, P., "Solver and Turbulence Model Upgrades to OVERFLOW 2 for Unsteady and High-Speed Applications," AIAA Paper 2006-2824, June 2006.

[3]Johnson, W., "Rotorcraft Aerodynamics Models for a Comprehensive Analysis," American Helicopter Society 54^{th} Annual Forum Proceedings, 1998.

[4]Tung, C., Caradonna, F., and Johnson, W., "The Prediction of Transonic Flows on an Advancing Rotor," American Helicopter Society 40^{th} Annual Forum Proceedings, 1984.

[5]Biedron, R. T. and Lee-Rausch, E. M., "Rotor Airloads Prediction Using Unstructured Meshes and Loose CFD/CSD Coupling," AIAA Paper 2008-7341, August 2008.

[6]Anderson, W. K. and Bonhaus, D. L., "An Implicit Upwind Algorithm for Computing Turbulent Flows on Unstructured Grids," *Computers and Fluids*, Vol. 23, (1), 1994, pp. 1–22.

[7]Abras, J., *Enhancement of Aeroelastic Rotor Airloads Prediction Methods*, Ph.D. thesis, Georgia Institute of Technology, 2009.

[8]Sankaran, V., Sitaraman, J., Wissink, A., Datta, A., Jayaraman, B., Potsdam, M., Mavriplis, D., Yang, Z., O'Brien, D., Saberi, H., Cheng, R., Hariharan, N., and Strawn, R., "Application of the Helios Computational Platform to Rotorcraft Flowfields," AIAA Paper 2010-1230, January 2010.

[9]Bondi, M. J. and Bjorkman, W. S., "Trends User's Guide and Reference Manual," NASA TM 108806, June 1994.

[10]Bousman, W. G. and Kufeld, R. M., "UH-60A Airloads Catalog," NASA TM 2005-212827, August 2005.

[11]Biedron, R. T. and Thomas, J. L., "Recent Enhancements To The FUN3D Flow Solver For Moving Mesh Applications," AIAA Paper 2009-1360, January 2009.

[12]Noack, R. W., "DiRTlib: A Library to Add an Overset Capability to Your Flow Solver," AIAA Paper 2005-5116, June 2005.

[13]Noack, R. W., Bogar, D. A., Kunz, R. F., and Carrica, P. M., "SUGGAR++: An Improved General Overset Grid Assembly Capability," AIAA Paper 2009-3992, June 2009.

[14]O'Brien, D., *Analysis of Computational Modeling Techniques for Complete Rotorcraft Configurations*, Ph.D. thesis, Georgia Institute of Technology, 2006.

[15]Pirzadeh, S., "Three-Dimensional Unstructured Viscous Grids by the Advancing Front Method," *AIAA Journal*, Vol. 34, (1), January 1996, pp. 43–49.

[16]Pirzadeh, S. Z., "Advanced Unstructured Grid Generation for Complex Aerodynamic Application," AIAA Paper 2008-7178, August 2008.

[17]Thomas, J. L., Diskin, B., and Rumsey, C. L., "Towards Verification of Unstructured-Grid Solvers," AIAA Paper 2008-0666, January 2008.

[18]Roe, P. L., "Approximate Riemann Solvers, Parameter Vectors, and Difference Schemes," *Journal of Computational Physics*, Vol. 43, 1981, pp. 357–372.

[19]Spalart, P. R. and Allmaras, S. R., "A One-Equation Turbulence Model for Aerodynamic Flows," *La Recherche Aerospatiale,* No. 1, 1994, pp. 5–21.

[20]Vatsa, V. and Carpenter, M. H., "Higher-Order Temporal Schemes with Error Controllers for Unsteady Navier-Stokes Equations," AIAA Paper 2005-5245, June 2005.

[21]Vatsa, V. N., Carpenter, M. H., and Lockard, D. P., "Re-evaluation of an Optimized Second Order Backward Difference (BDF2OPT) Scheme for Unsteady Flow Applications," AIAA Paper 2010-0122, January 2010.

[22]Menter, F. R., "Two-Equation Eddy-Viscosity Turbulence Models for Engineering Applications," *AIAA Journal*, Vol. 32, (8), 1994, pp. 1598–1605.

[23]Lynch, E. and Smith, M., "Hybrid RANS-LES Turbulence Models on Unstructured Grids," AIAA Paper 2008-3854, June 2008.

[24]Sitaraman, J., Potsdam, M., Jayaraman, B., Datta, A., Wissink, A., Mavriplis, D., and Saberi, H., "Rotor Loads Prediction Using Helios: A Multi-Solver Framework for Rotorcraft CFD/CSD Analysis," AIAA Paper 2011-1123, January 2011.

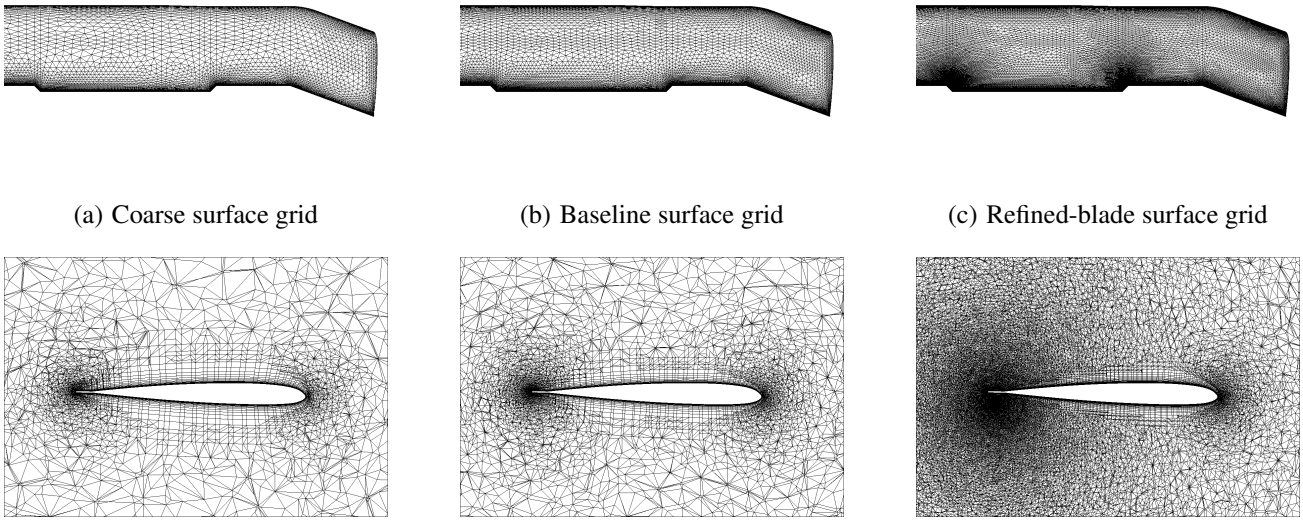

(a) Coarse surface grid (b) Baseline surface grid (c) Refined-blade surface grid

(d) Coarse volume slice (e) Baseline volume slice (f) Refined-blade volume slice

Fig. 1. Comparison of UH-60 blade surface grids and volume slices at $r/R = 0.865$.

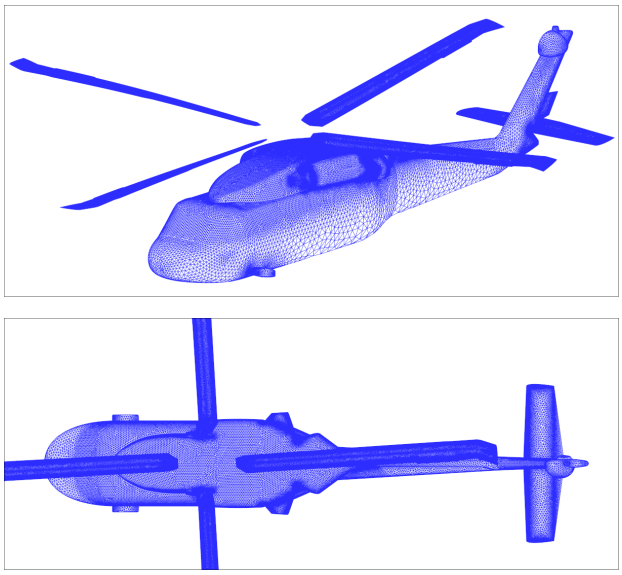

Fig. 2. Surface grids corresponding to the 19 million node baseline volume mesh.

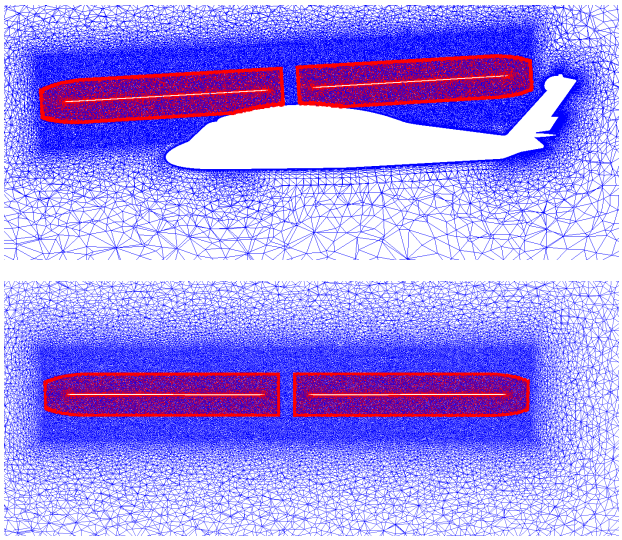

Fig. 3. Slice through the baseline volume grid systems, with and without fuselage (19 million and 18 million grid points, respectively).

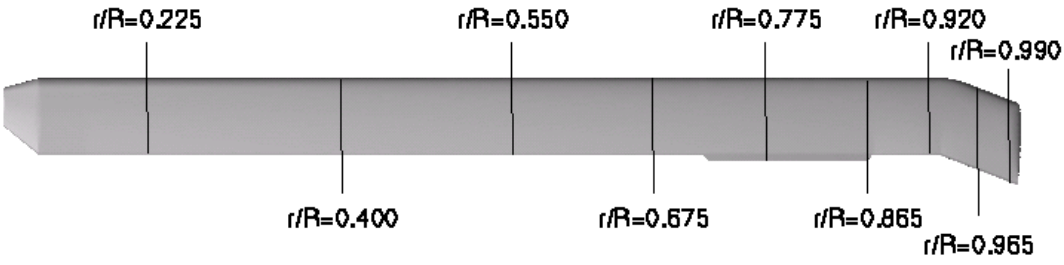

Fig. 4. Blade radial stations for which flight airloads are available.

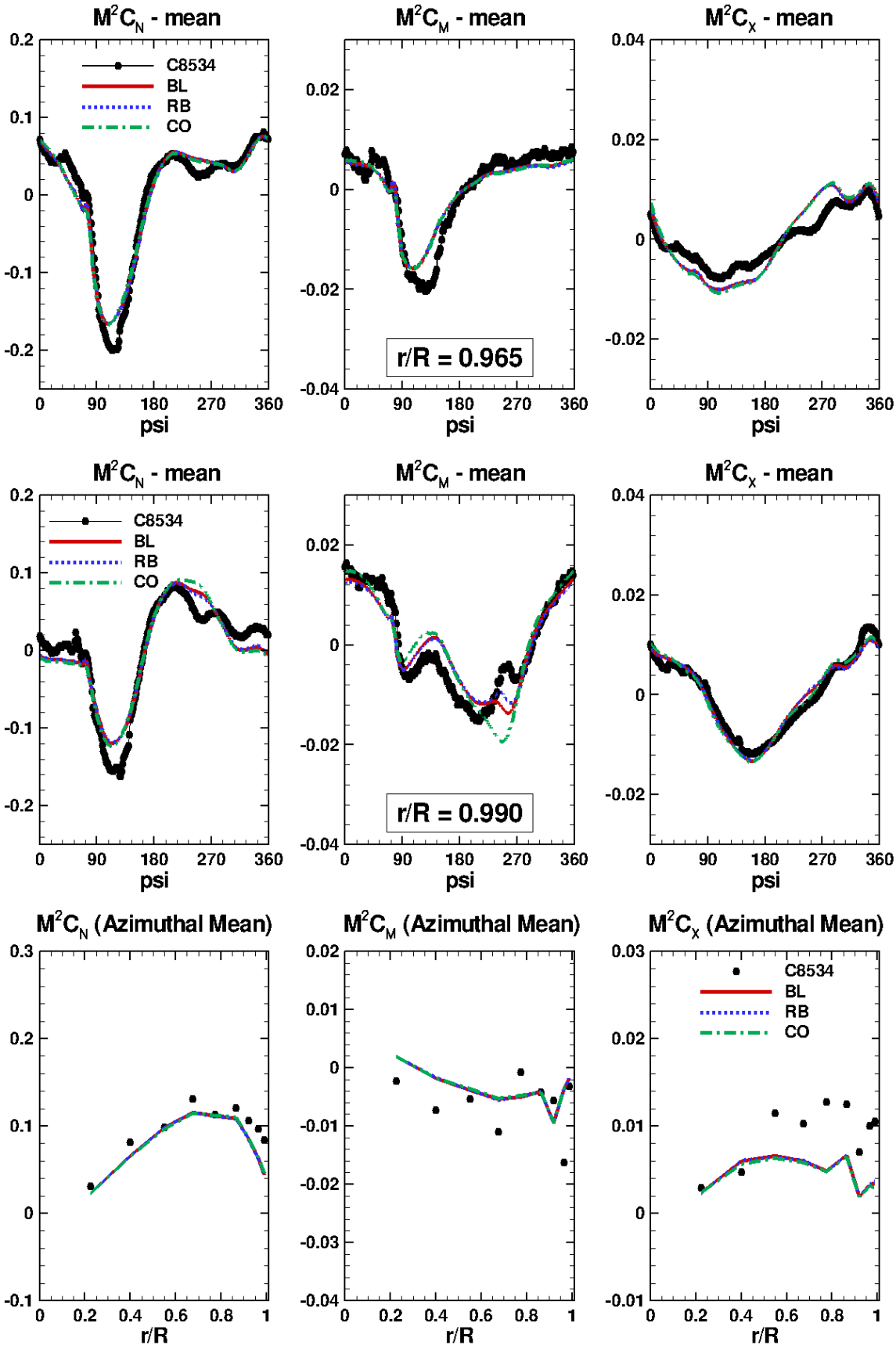

Fig. 5. Effect of mesh refinement on computed airloads (isolated rotor) at r/R = 0.965, and r/R = 0.990, together with azimuthal averages, Counter 8534. CO: 6.9 million nodes, BL: 17.6 million nodes, RB: 37.4 million nodes; all mixed-element meshes.

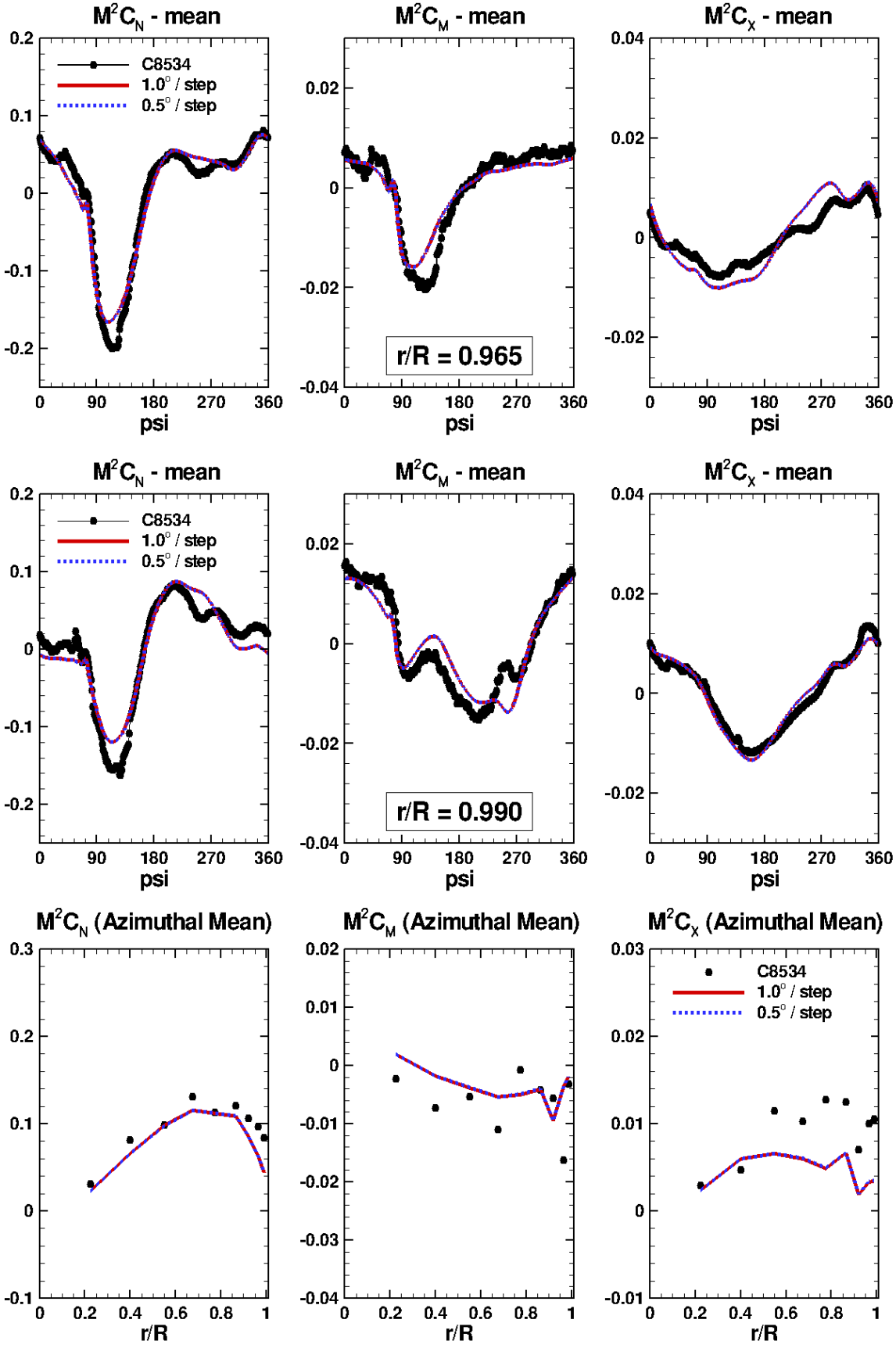

Fig. 6. Effect of time step refinement on computed airloads (isolated rotor) at r/R = 0.965, and r/R = 0.990, together with azimuthal averages, Counter 8534.

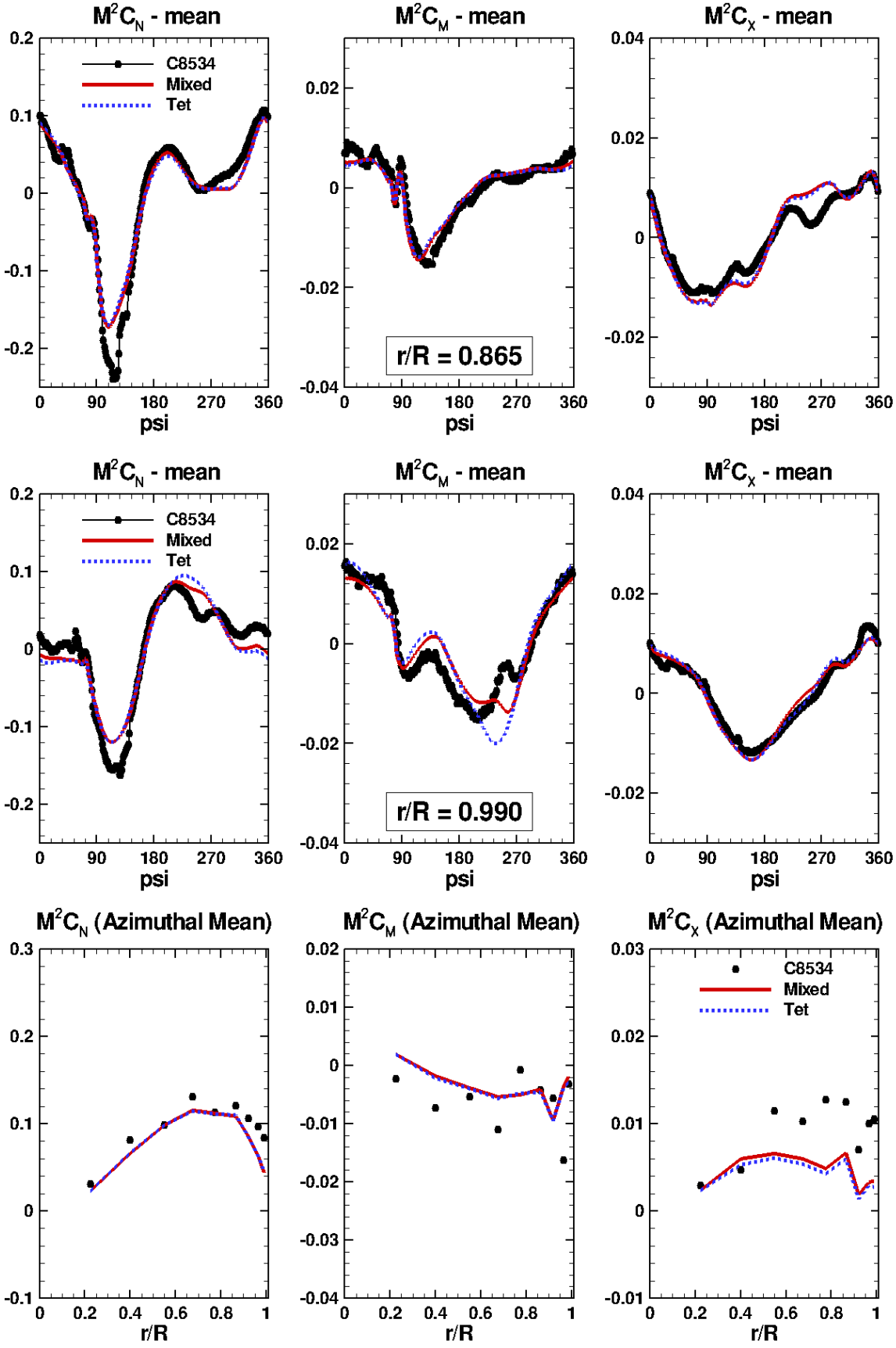

Fig. 7. Comparison of computed (isolated rotor) and measured airloads at r/R = 0.865, r/R=0.990, together with azimuthal averages, Counter 8534. Computations performed on mixed-element and tetrahedral meshes.

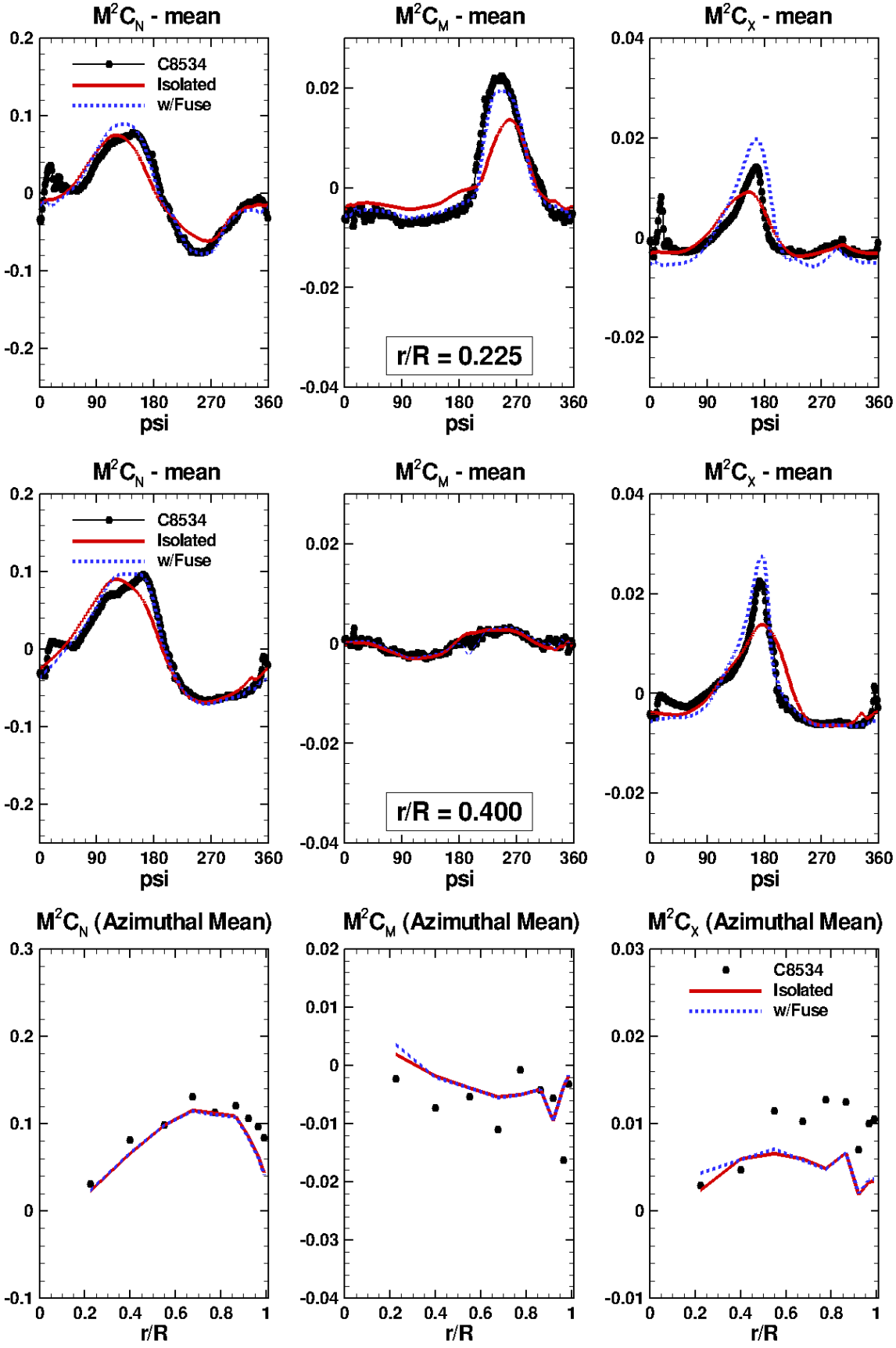

Fig. 8. Effect of fuselage on computed airloads at r/R = 0.225, and r/R = 0.400, together with azimuthal averages, Counter 8534. Computations performed on mixed-element meshes.

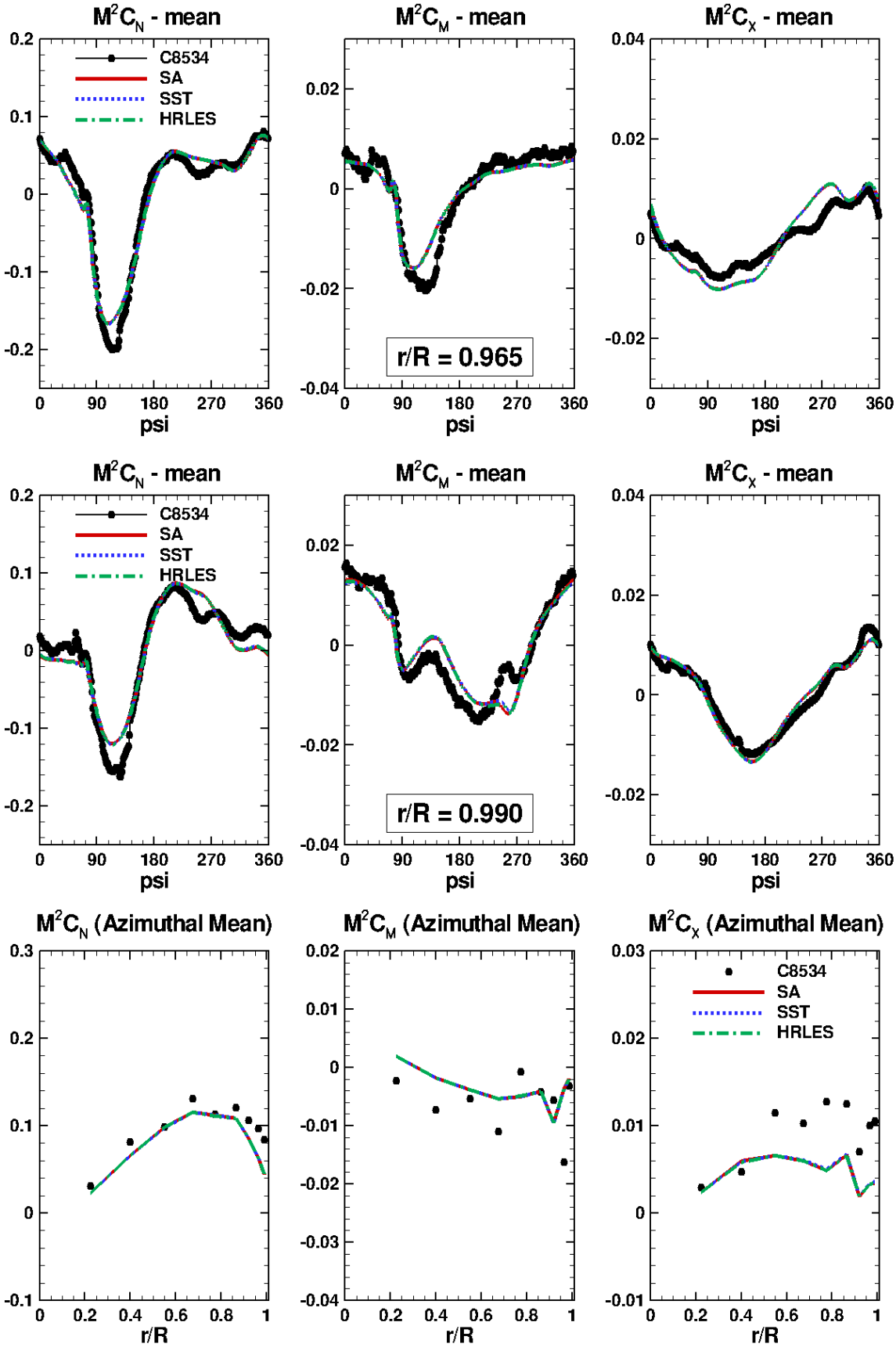

Fig. 9. Effect of turbulence model variation on computed airloads (isolated rotor) at r/R = 0.965, and r/R = 0.990, together with azimuthal averages, Counter 8534. Computations performed on the 17.6 million node mixed-element mesh, with a time step corresponding to 1.0°.

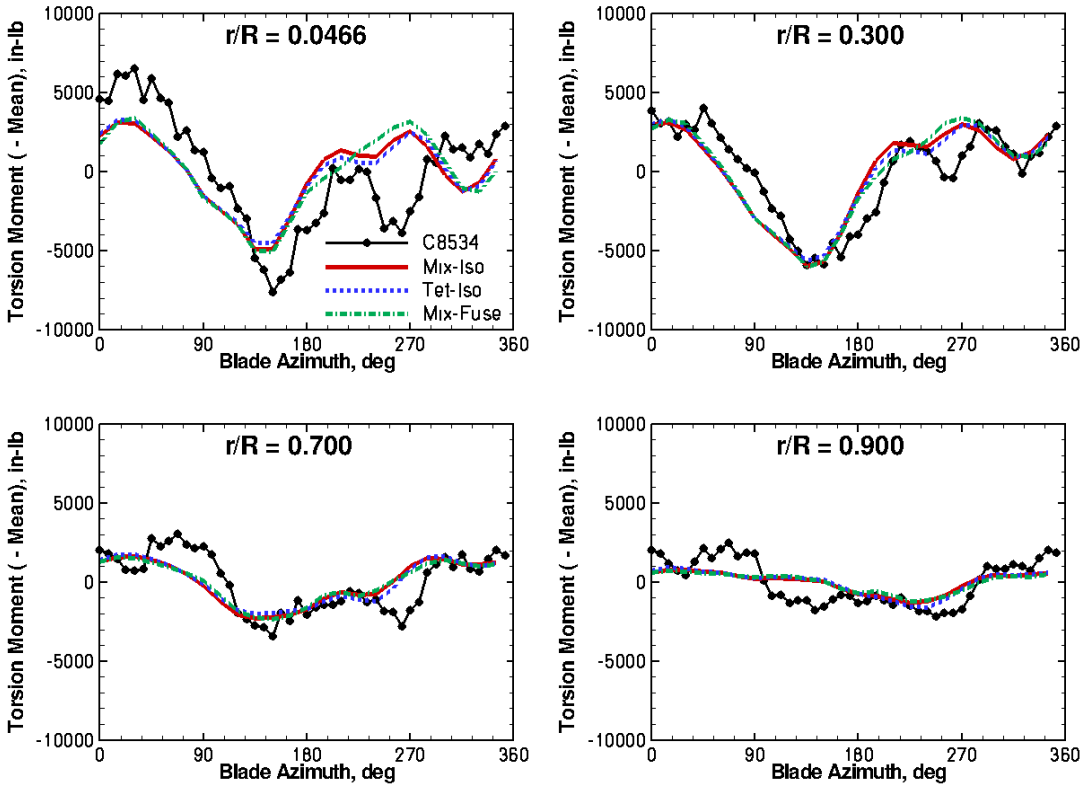

Fig. 10. Effect of selected CFD mesh variations on the computed torsional moment (means removed), Counter 8534.

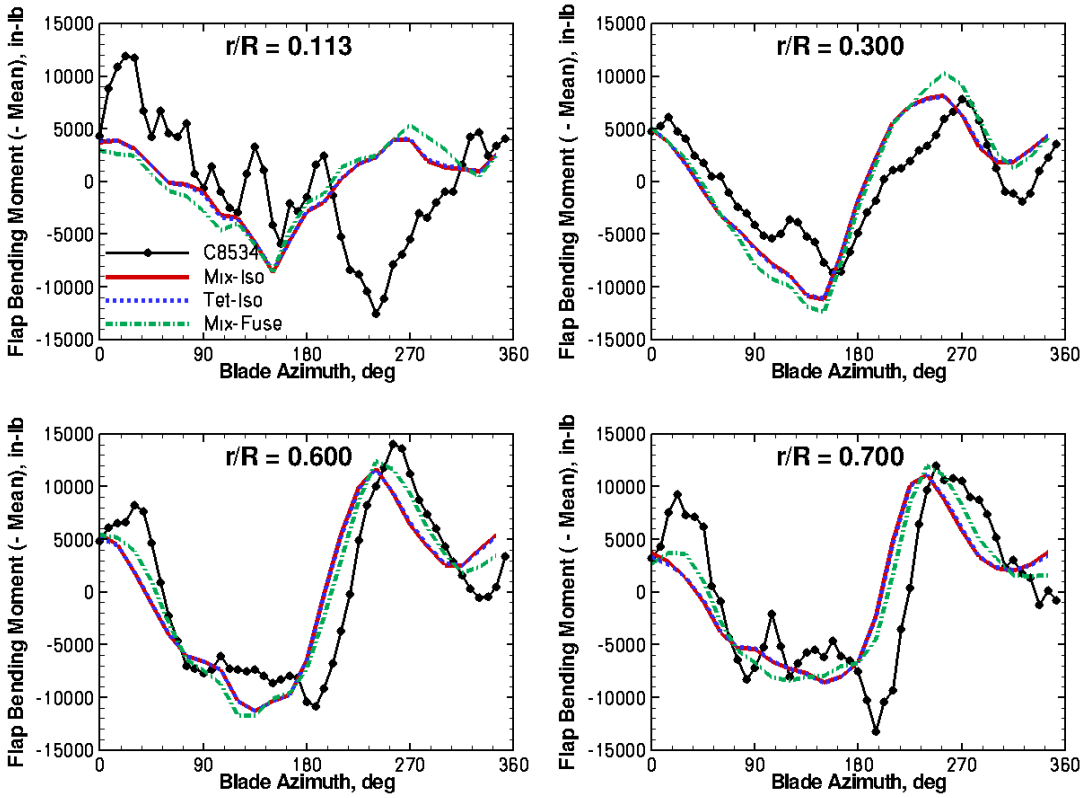

Fig. 11. Effect of selected CFD mesh variations on the computed normal bending moment (means removed), Counter 8534.

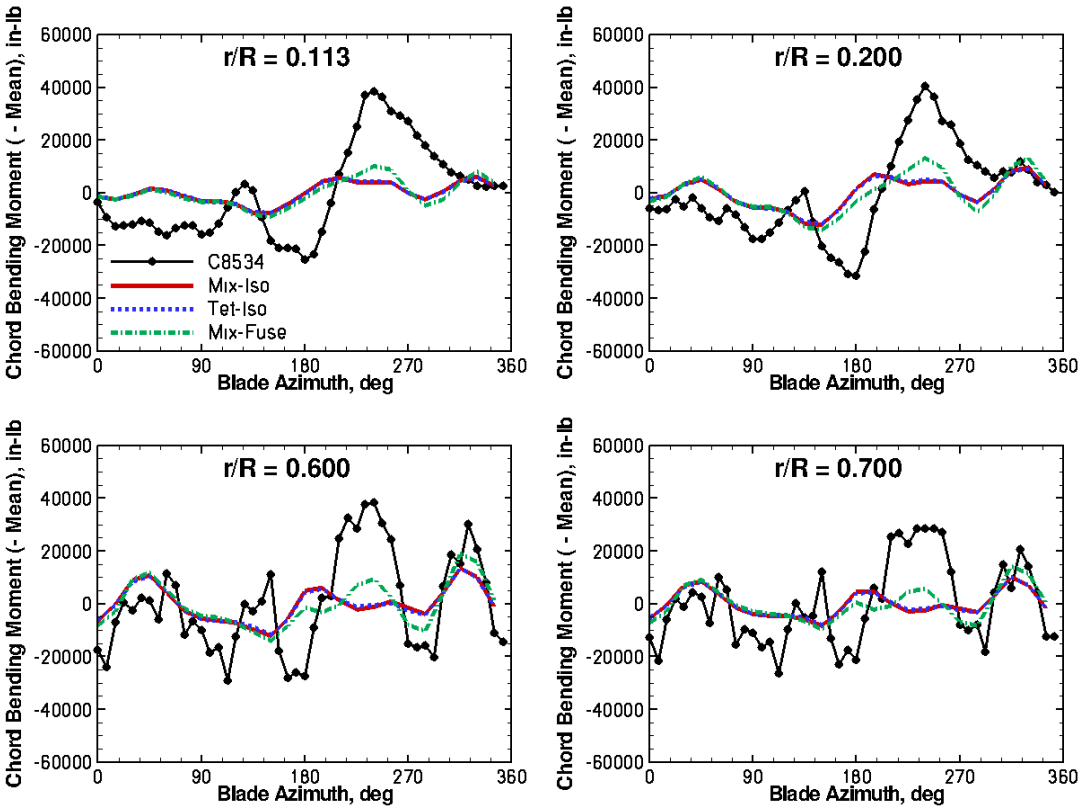

Fig. 12. Effect of selected CFD mesh variations on the computed edgewise bending moment (means removed), Counter 8534.

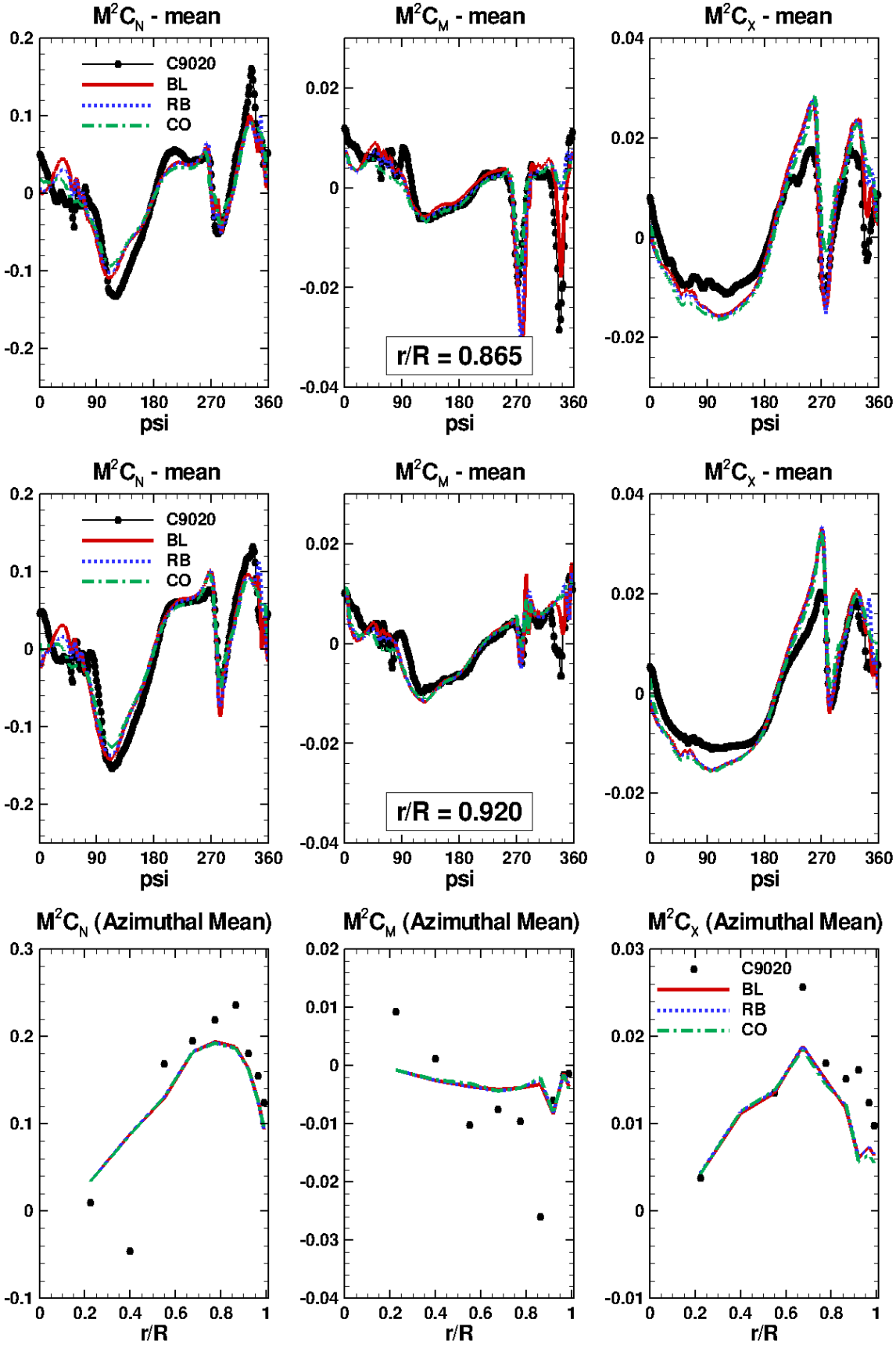

Fig. 13. Effect of mesh refinement on computed airloads (isolated rotor) at r/R = 0.865, and r/R = 0.920, together with azimuthal averages, Counter 9020. CO: 6.9 million nodes, BL: 17.6 million nodes, RB: 37.4 million nodes).

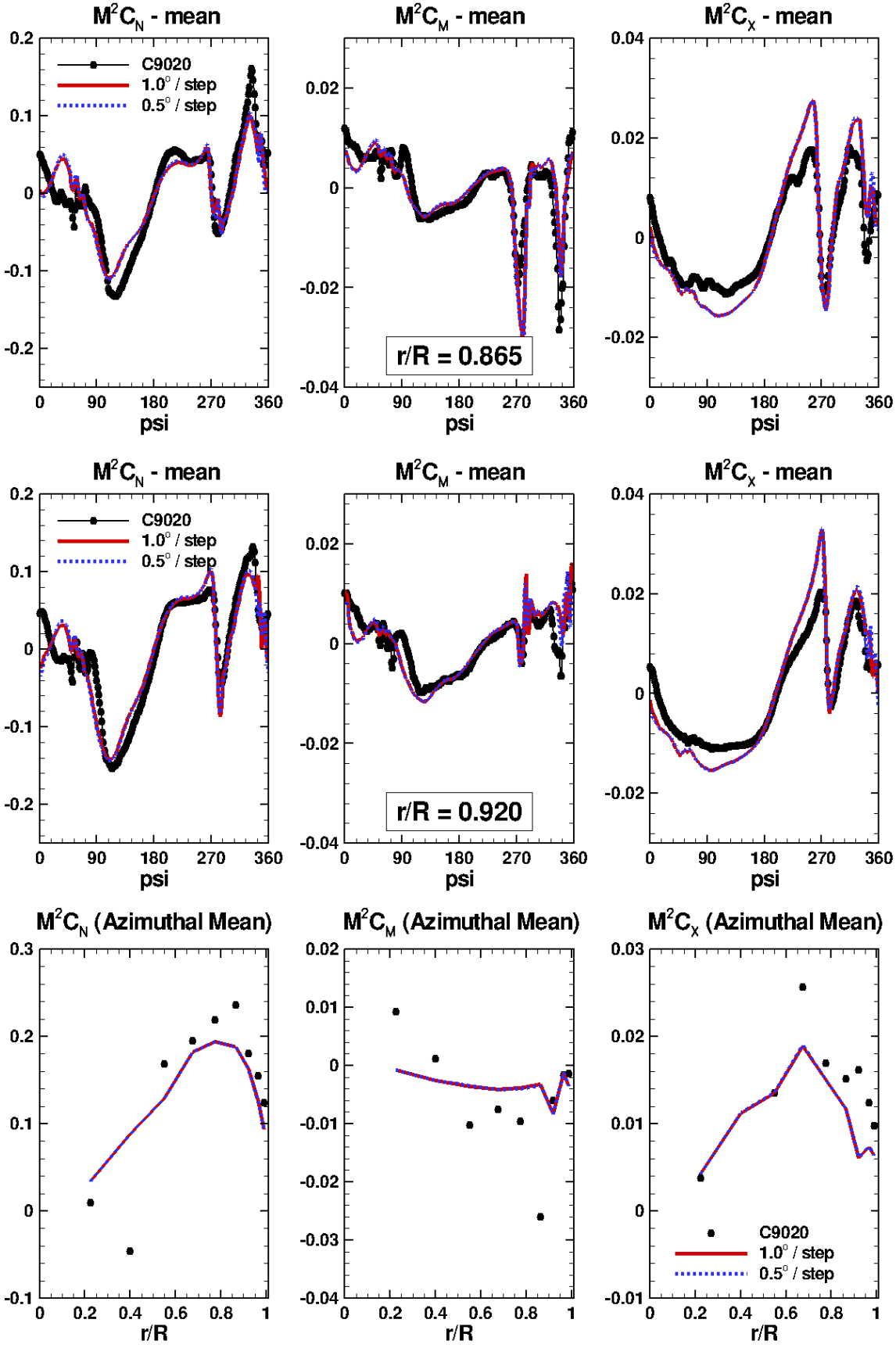

Fig. 14. Effect of time step refinement on computed airloads (isolated rotor) at r/R = 0.865, and r/R = 0.920, together with azimuthal averages, Counter 9020. Computations performed on the 37.6 million node mesh

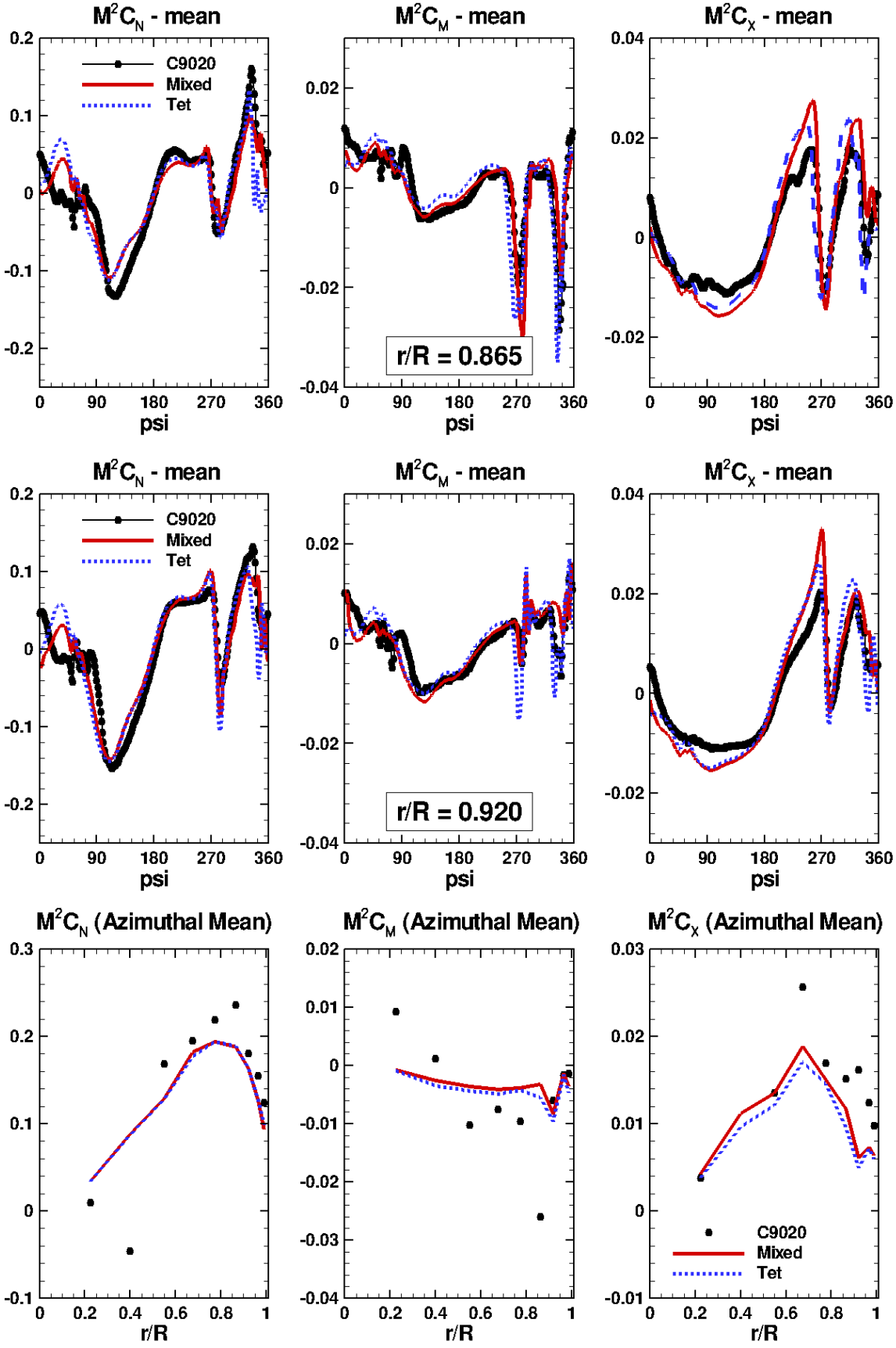

Fig. 15. Comparison of computed (isolated rotor) and measured airloads at r/R = 0.865, and r/R = 0.920, together with azimuthal averages, Counter 9020. Computations performed on mixed-element and tetrahedral meshes.

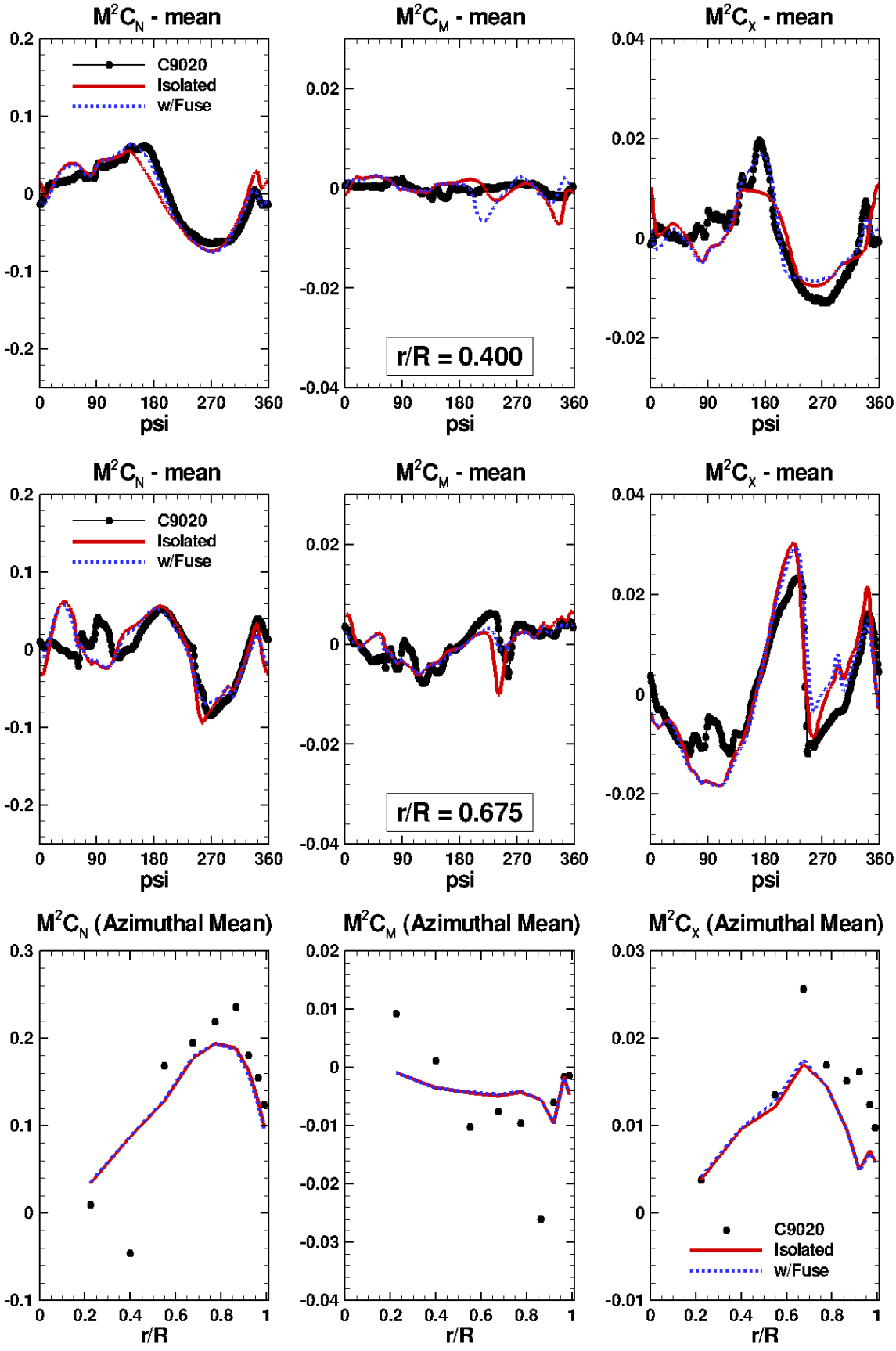

Fig. 16. Effect of fuselage on computed airloads at r/R = 0.400, and r/R = 0.675, together with azimuthal averages, Counter 9020.

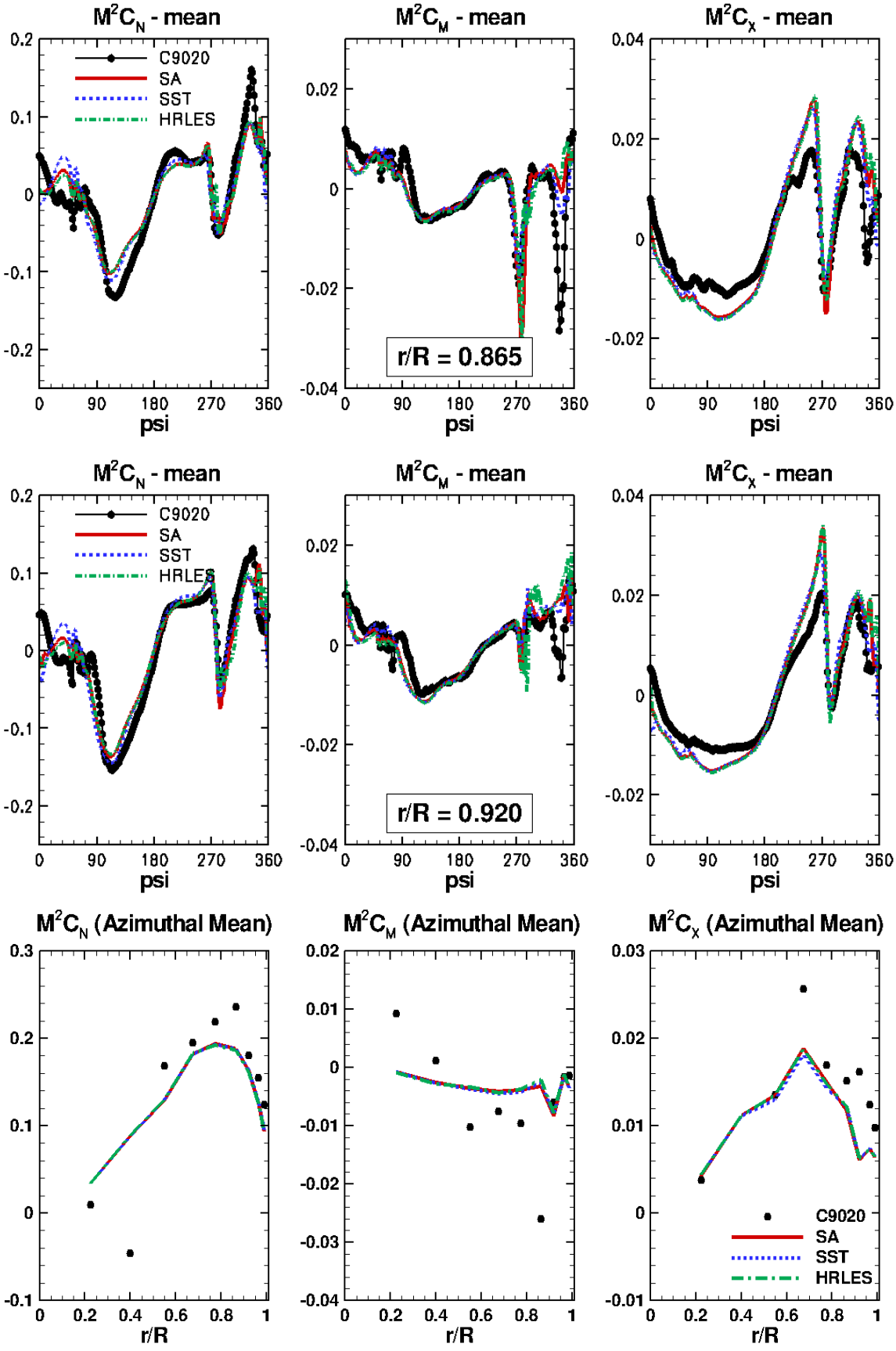

Fig. 17. Effect of turbulence model on computed airloads (isolated rotor) at r/R = 0.865, and r/R = 0.920, together with azimuthal averages, Counter 9020. Computations performed on the 37.6 million node mixed-element mesh, with a time step corresponding to 0.5°**.**

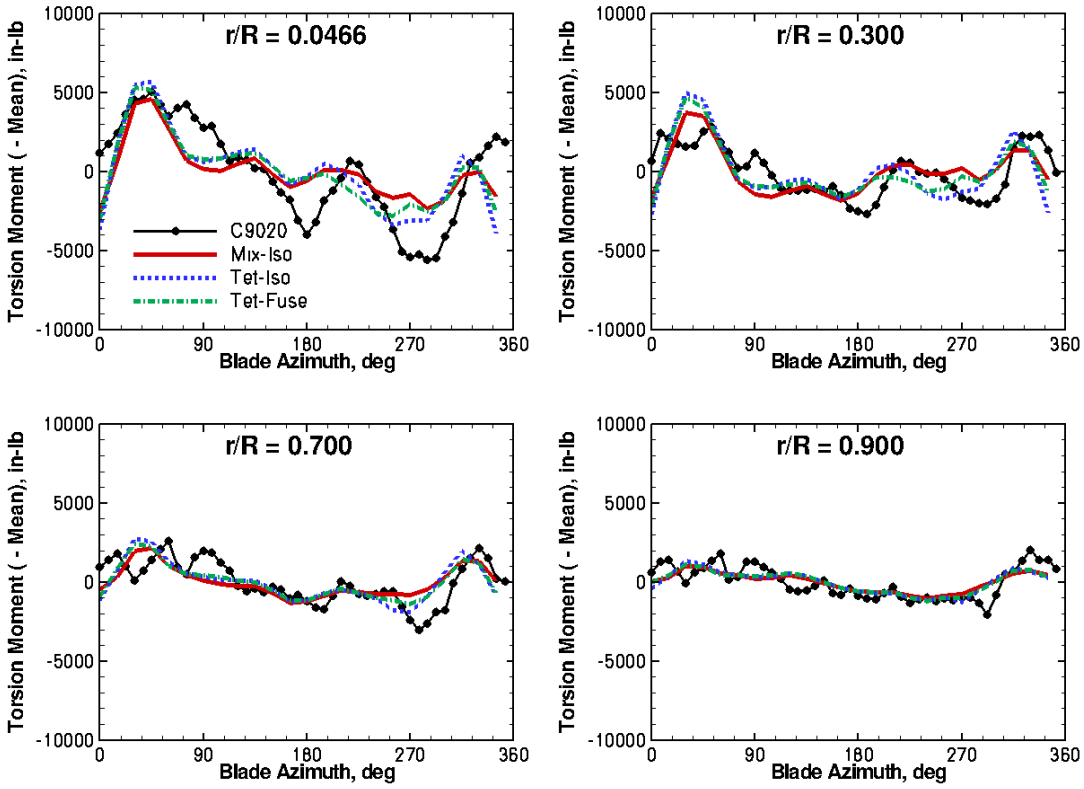

Fig. 18. Effect of selected CFD mesh variations on the computed torsional moment (means removed), Counter 9020.

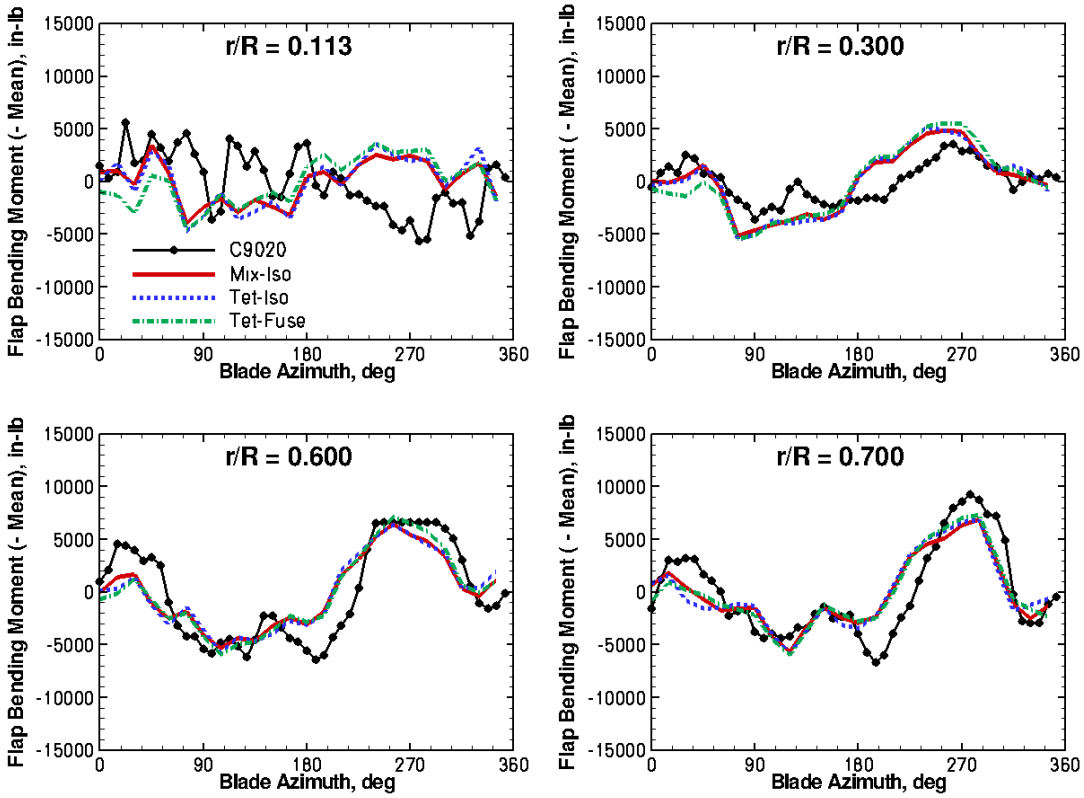

Fig. 19. Effect of selected CFD mesh variations on the computed normal bending moment (means removed), Counter 9020.

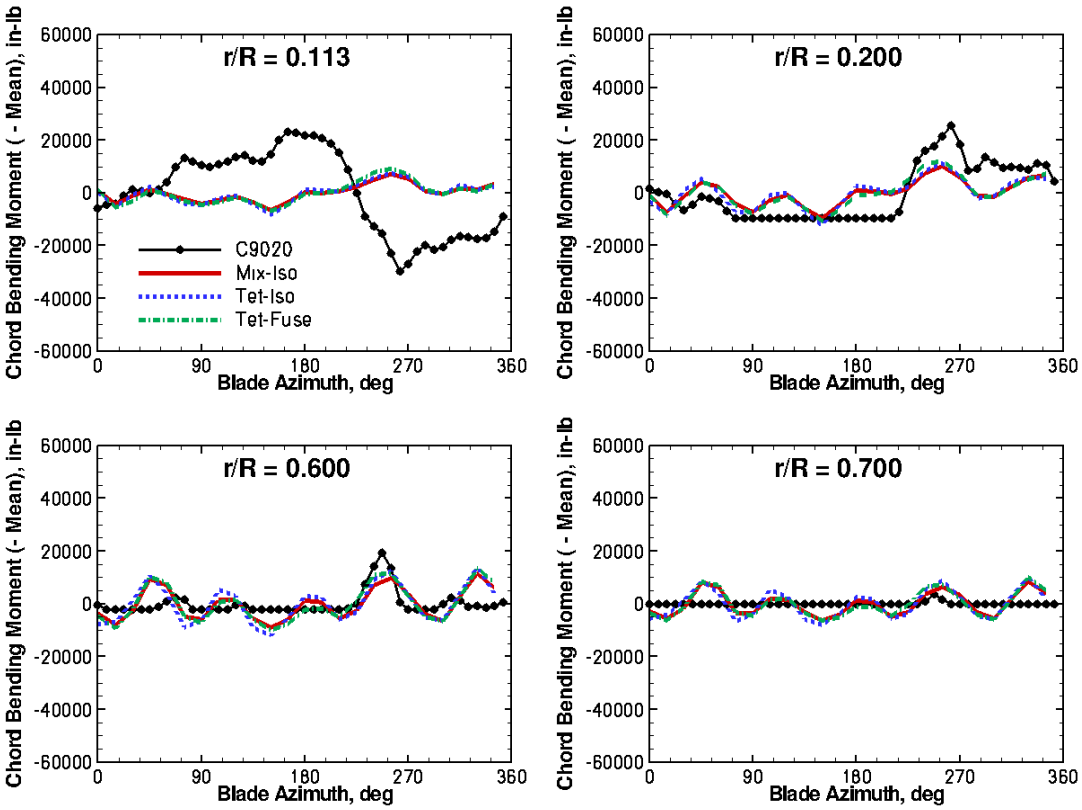

Fig. 20. Effect of selected CFD mesh variations on the computed edgewise bending moment (means removed), Counter 9020.